Electronic Supplementary Material (ESI) for Nanoscale.

Supplementary Information

Bismuth-Nickel bimetal Nanosheets with Porous Structure for Efficient Hydrogen production in Neutral and Alkaline media

Xueping Yu,‡[a] Li Qu,‡[a] Carmen Lee,[b] Juan Peng,*[a] Qingyu Yan,*[b] Hongcun Bai,[a] Min Yao,[a]

[a]College of Chemistry and Chemical Engineering, State Key Laboratory of High-efficiency Utilization of Coal and Green Chemical Engineering, Yinchuan 750021, P. R. China

[b]Center for Programmable Materials, School of Materials Science and Engineering, Nanyang Technological University, Singapore 639798, Singapore

[c] Institute of Materials Research and Engineering, A*STAR, 2 Fusionopolis Way, Innovis, #08-03, Singapore 138634, Singapore

Table S1. The ICP-OES results for alloys.

Different concentrations of $NiSO_4.7H_2O$	Bi:Ni atomic (%)	Sample name
0.01 M	86.5 13.5	$Bi_{86.5}Ni_{13.5}$
0.02 M	84.8 15.2	$Bi_{84.8}Ni_{15.2}$
0.03 M	80.1 19.9	$Bi_{80.1}Ni_{19.9}$
0.04 M	76.2 23.8	$Bi_{76.2}Ni_{23.8}$

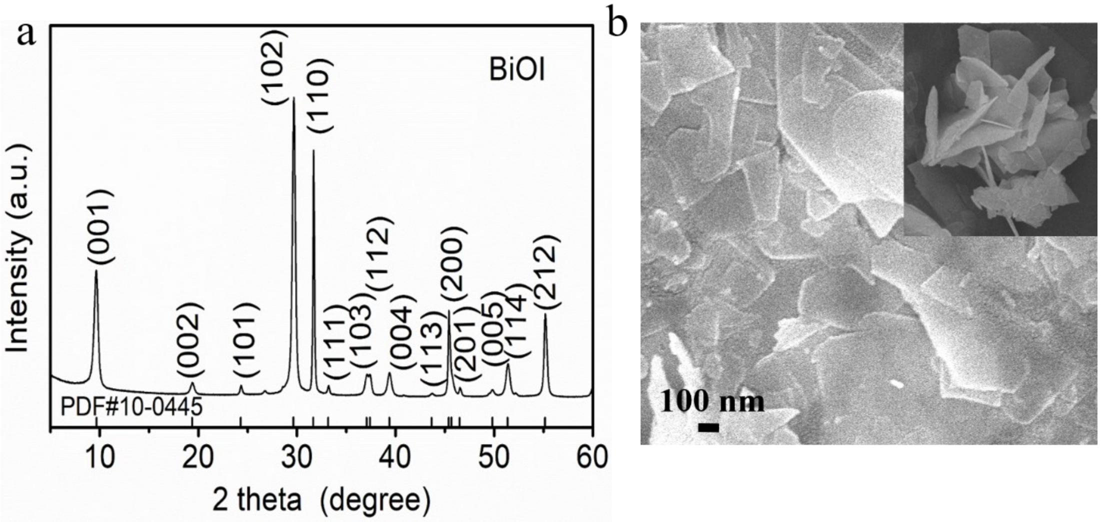

Fig. S1 Structural characterizations of BiOI nanosheet (a) XRD pattern; (b) SEM image

Table S2. The XRD and HRTEM results of Bi-Ni alloy

Samples	2θ/degree (110)	$d_{(110)}$ spacing (nm)	Strain (%)
Bi (PDF#44-1246)	39.62	0.227	-
$Bi_{84.8}Ni_{15.2}$ alloy	39.91	0.222	2.20
$Bi_{80.1}Ni_{19.9}$ alloy	40.05	0.212	6.61

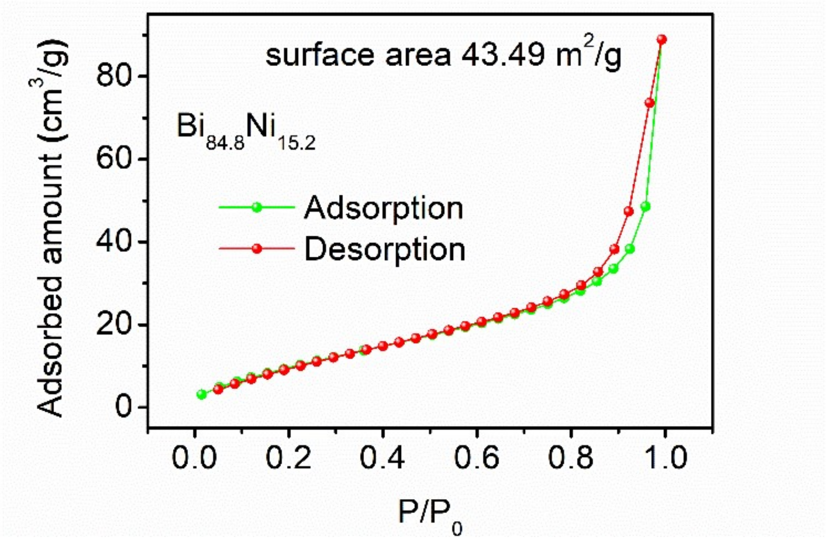

Fig. S2 N_2 adsorption-desorption isotherm of $Bi_{84.8}Ni_{15.2}$ alloy.

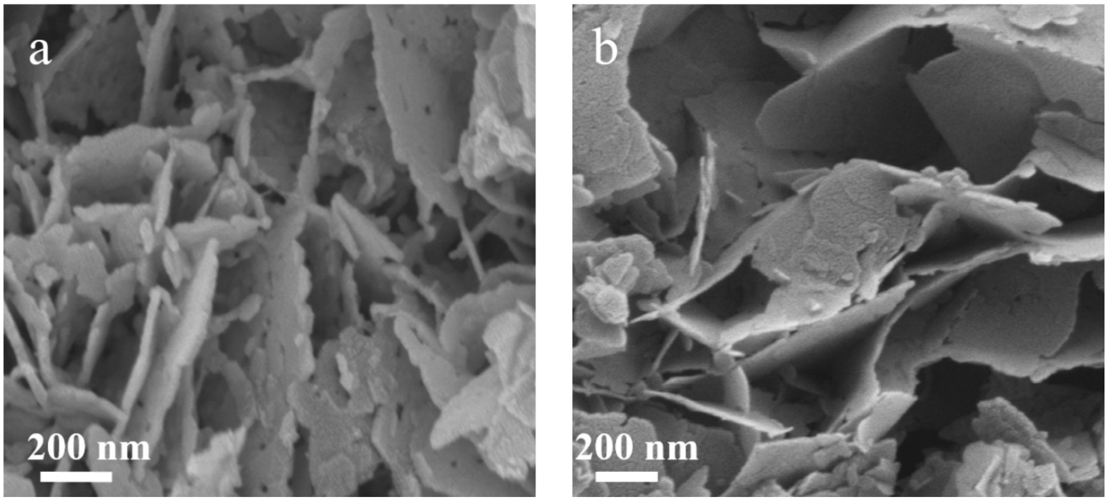

Fig. S3 SEM images of Bi nanosheets obtained via electrochemical reduction in Na_2SO_4 (a); $NaHCO_3$ aqueous solution (b).

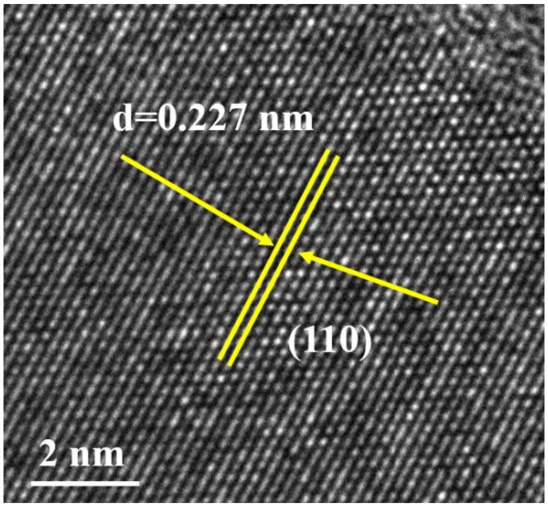

Fig. S4 HRTEM image of Bi nanosheet.

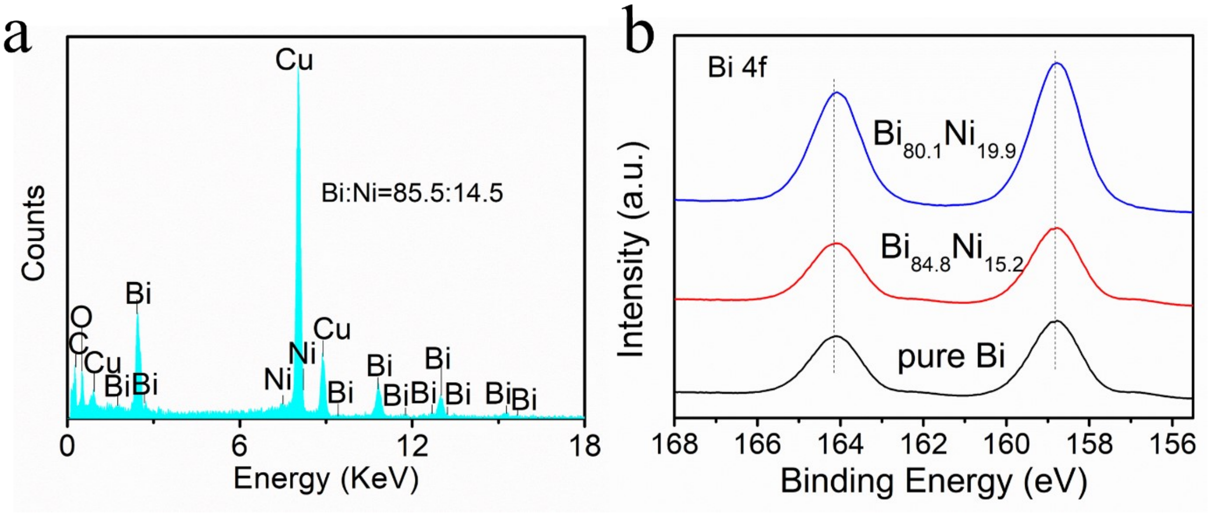

Fig. S5 (a) The EDS spectrum of $Bi_{84.8}Ni_{15.2}$ alloy; (b) XPS spectra of $Bi_{80.1}Ni_{19.9}$ alloy, $Bi_{84.8}Ni_{15.2}$ and Bi 4f.

In Fig. S6a, the XRD pattern of $Bi_{80.1}Ni_{19.9}$ shows the peaks slightly shifted relative to Bi (PDF#44-1246) and Ni (PDF#04-0850) peaks. In addition, no Bi and Ni-related diffraction peaks are observed, suggesting the formation of the alloy phase. The $Bi_{80.1}Ni_{19.9}$ alloy presents mesoporous structure, as shown from the image of Fig. S6b. In Fig. S6c,d, the lattice spacing of $Bi_{80.1}Ni_{19.9}$ alloy is 0.212 nm, which is much smaller than those of Bi (0.227 nm; Fig. S4) and down-regulated by 6.61% as compared to Bi (Table S2). The result suggests lattice shrinkage which could be due to the introduction of nickel atoms. Figs. S6e-g exhibits uniform distribution of Bi and Ni atoms in mesoporous $Bi_{80.1}Ni_{19.9}$ alloy. SAED exhibits the polycrystalline properties of $Ni_{80.1}Bi_{19.1}$ alloy (Fig. S6h). Fig. S6i presents the elemental composition of the mesoporous $Bi_{80.1}Ni_{19.9}$ alloy which includes Ni, Bi and O. The O element originated from the air and the ineluctable surface oxidation of samples.

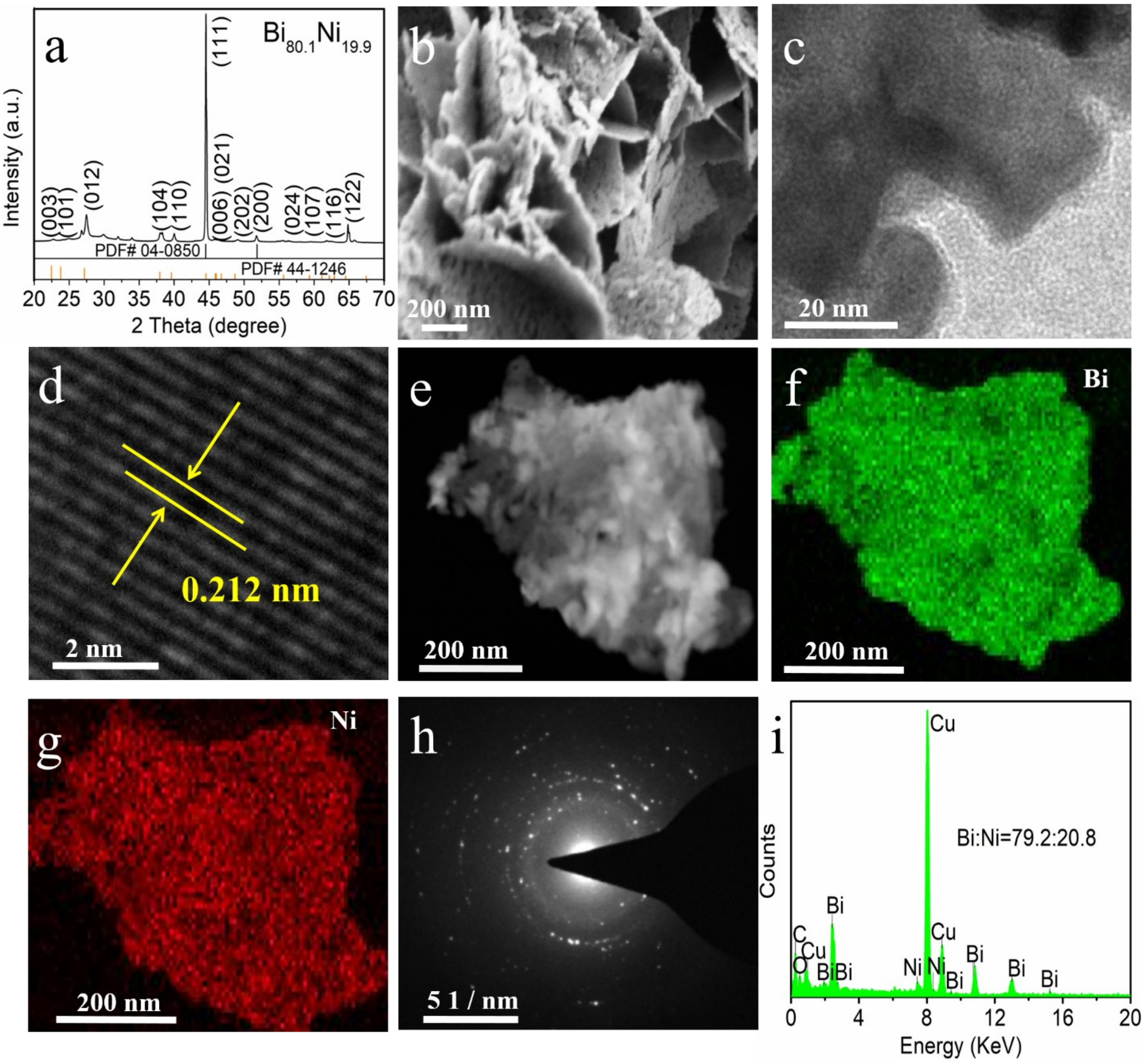

Fig. S6 Structural characterizations of $Bi_{80.1}Ni_{19.9}$ alloy (a) XRD patterns; (b) SEM; (c) TEM; (d) HRTEM; (e) HAADF-STEM; (f-g) EDS mapping images; (h) SAED; (i) EDS spectrum.

The Bi 4f spectrum shows that both the oxidation state (Bi^{3+}) and metallic state (Bi^0) coexist on the surface of $Bi_{80.1}Ni_{19.9}$ alloy (Fig. S7a). For Ni 2p spectrum (Fig. S7b), the binding energies at 856.18 (Ni $2p_{3/2}$) and 874.68 eV (Ni $2p_{1/2}$) with characteristic satellite peaks at 861.28 and 879.18 eV indicate the existence of both Ni^{2+} and Ni^0 states [1].

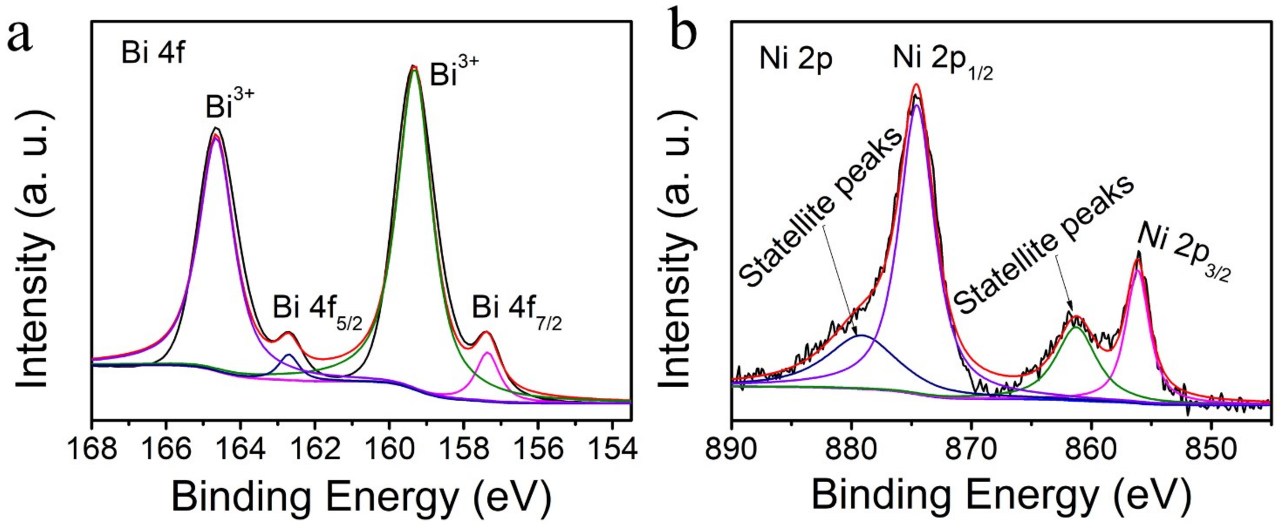

Fig. S7 XPS spectrum of $Bi_{80.1}Ni_{19.9}$ alloy (a) Bi 4f; (b) Ni 2p.

Table S3. Comparison of HER performance with reported bimetallic catalysts in 1.0 M KOH.

Samples	Overpotential (mV)@10 mA/cm^2	Tafel slop (mV/dec)	References
RuNi alloy@SC	93	96	[2]
PtNi/rGO	112	72	[3]
CuFe/NF	158	62.2	[4]
Au_3Pt/NF	40.1	42.3	[5]
$Ni_{1.87}Mo_{0.13}P$	101	49.5	[6]
Ru_1Co_2	188	111.5	[7]
$Cu_{95}Ti_5$	50	110	[8]
NiMoN	109	95	[9]
$(Co_{0.52}Fe_{0.48})_2P$	~95	40	[10]
FeCo-600	262	74	[11]
$NiCo_2Px$	58	34.3	[12]
NiCoP/NPC	128	70	[13]
$Bi_{84.8}Ni_{15.2}$	56	115	This work

Note: RuNi alloy@SC: RuNi alloy implanted with S-doped defective carbon; PtNi/rGO: platinum–nickel alloy nanoparticle–supported reduced graphene oxide (rGO); CuFe/NF: CuFe bifunctional electrocatalyst on Ni foam; Au_3Pt/NF: porous Au_3Pt film on Ni foam. FeCo-600: FeCo alloy nanoparticles encapsulated in highly nitrogen-doped (8.2 atom %) graphene layers by direct annealing of MOF nanoparticles at 600 °C in N_2; NiCoP/NPC: bimetallic nickel cobalt phosphide and N, P-doped carbon composite.

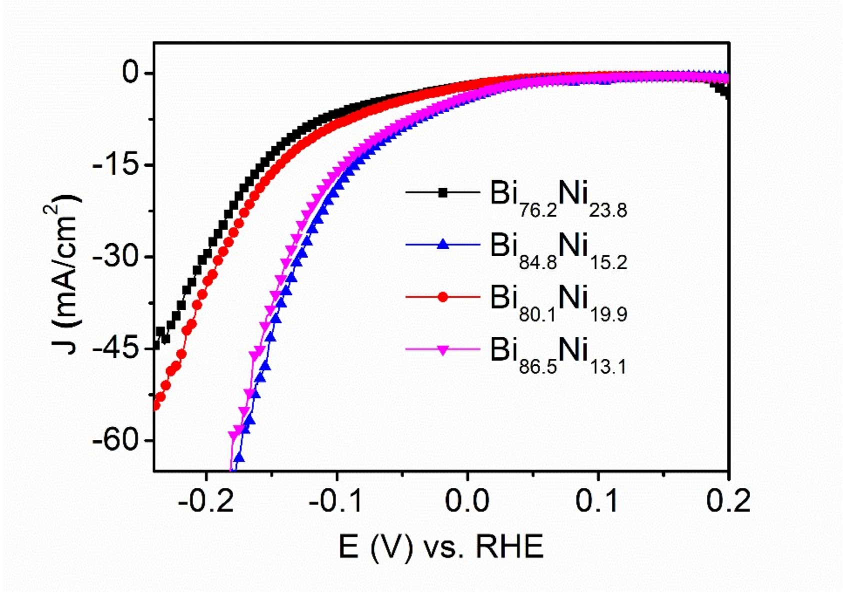

Fig. S8 Polarization curves of four alloys for HER in 1.0 M KOH.

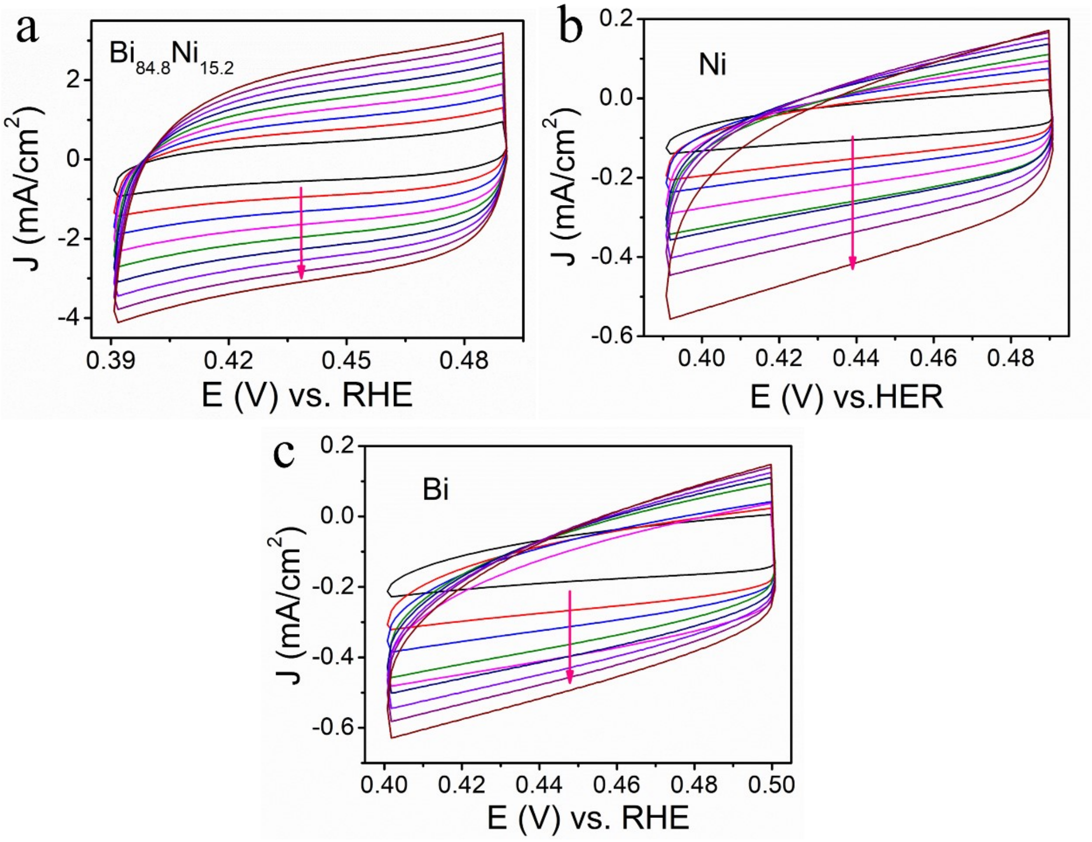

Fig. S9 CV at 20-180 mV/s in 1.0 M KOH (a) $Bi_{84.8}Ni_{15.2}$; (b) Ni; (c) Bi.

The ECSA was calculated according to the reported work [14]

$$ECSA = C_{dl}/C_s$$

C_s: specific capacitance (0.040 mF/cm^2).

In 1.0 M KOH

$$ECSA_{(Bi_{84.8}Ni_{15.2})} = \frac{13.65 \times 0.07}{0.040} = 23.89\ cm^2$$

$$ECSA_{(Ni)} = \frac{1.64 \times 0.07}{0.040} = 2.87\ cm^2$$

$$ECSA_{(Bi)} = \frac{0.83 \times 0.07}{0.040} = 1.45\ cm^2$$

In 1.0 M PBS (pH=7.0)

$$ECSA_{(Bi_{80.1}Ni_{19.9})} = \frac{15.45 \times 0.07}{0.040} = 27.04\ cm^2$$

$$ECSA_{(Ni)} = \frac{8.75 \times 0.07}{0.040} = 15.31\ cm^2$$

$$ECSA_{(Bi)} = \frac{0.71 \times 0.07}{0.040} = 1.24\ cm^2$$

The roughness factors (RF) were calculated according to reference [15]

$$RF = \frac{ECSA}{GSA}$$

ECSA: electrochemical surface area; GSA geometrical surface area.

In 1.0 M KOH

$$RF_{(Bi_{84.8}Ni_{15.2})} = \frac{23.89}{0.07} = 341.29$$

$$RF_{(Ni)} = \frac{2.87}{0.07} = 41.00$$

$$RF_{(Bi)} = \frac{1.45}{0.07} = 20.71$$

In 1.0 M PBS (pH=7.0)

$$RF_{(Bi_{80.1}Ni_{19.9})} = \frac{27.04}{0.07} = 386.29$$

$$RF_{(Ni)} = \frac{15.31}{0.07} = 218.71$$

$$RF_{(Bi)} = \frac{1.24}{0.07} = 17.7$$

TOF values were calculated to reference [16]

$$TOF = \frac{\#\ \text{total hydrogen turnover per geometric area}}{\#\ \text{active sites per geometric area}}$$

Total hydrogen turnover per geometric area

$$= (|j|\frac{mA}{cm^2})(\frac{1C/s}{1000\ mA})(\frac{1\ mol\ e^-}{96485.3\ C})(\frac{1\ mol}{2\ mol\ e^-})(\frac{6.022 \times 10^{23}\ molecules\ H_2}{1\ mol\ H_2})$$

$$= 3.12 \times \frac{\mathrm{H_2/s}}{\mathrm{cm^2}} \frac{mA}{cm^2}$$

Ni active site

$$= (\frac{catalyst\ loading\ per\ geometric\ area\ \left(x\ g/cm^2\right) * Ni\ wt\%}{Ni\ Mw(g/mol)}) \times (\frac{6.022 \times\ 10^{23}\ Ni\ atoms}{1mol\ Ni})$$

The Ni active site in Bi-Ni alloy can be calculated to be

Ni active sites in $Bi_{84.8}Ni_{15.2}$ $= (\frac{1.52 \times 10^{-5}}{58.69}) \times (\frac{6.022 \times 10^{23}\ Ni\ atoms}{1\ mol\ Ni}) = 1.56 \times 10^{17}$

Ni active sites in $Bi_{80.1}Ni_{19.9}$ $= (\frac{2.07 \times 10^{5}}{58.69}) \times (\frac{6.022 \times 10^{23}\ Ni\ atoms}{1\ mol\ Ni}) = 2.13 \times 10^{17}$

The TOFs of per site in Bi-Ni alloy can be calculated to be

TOF ($Bi_{84.8}Ni_{15.2}$) $= (\frac{3.12 \times 10^{15}}{1.56 \times 10^{17}}) \times |j\ | = 0.0208\ |j|$

TOF ($Bi_{80.1}Ni_{19.9}$)= $= (\frac{3.12 \times 10^{15}}{2.13 \times 10^{17}}) \times |j| = 0.0146|j|$

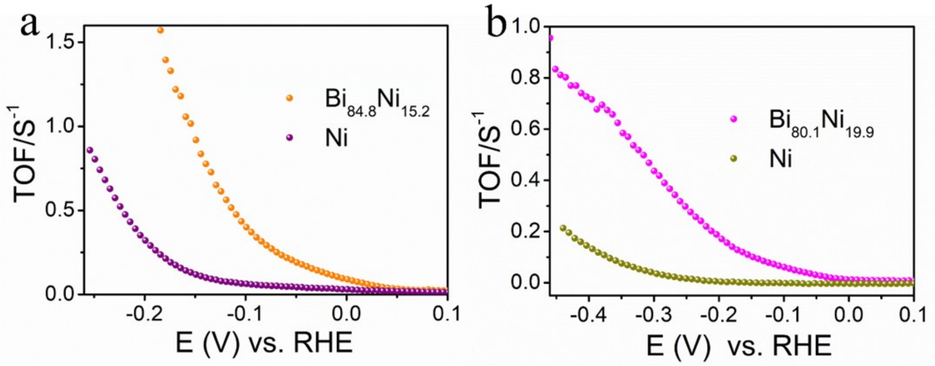

Fig. S10 Potential dependence of TOF value for HER (a) Ni and $Bi_{84.8}Ni_{15.2}$ alloy in 1.0 M KOH; (b) Ni and $Bi_{80.1}Ni_{19.9}$ alloy in 1.0 M PBS (pH=7.0).

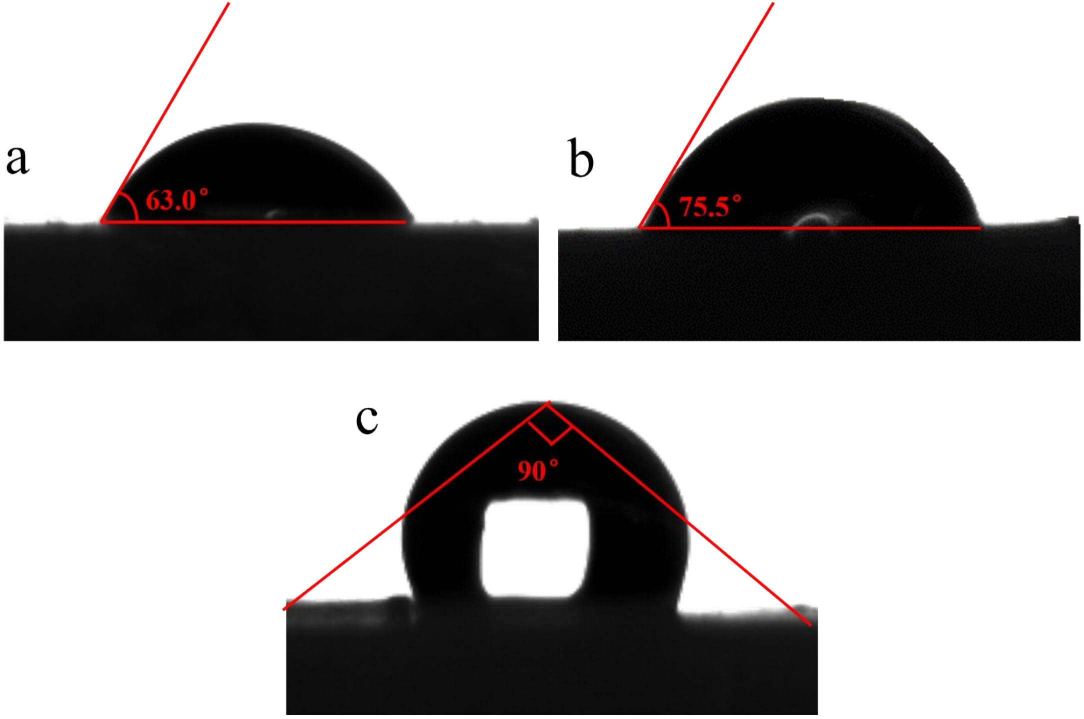

Fig. S11 Contact angle measurements (a) $Bi_{84.8}Ni_{15.2}$ alloy; (b) $Bi_{80.1}Ni_{19.9}$ alloy; (c) Bi.

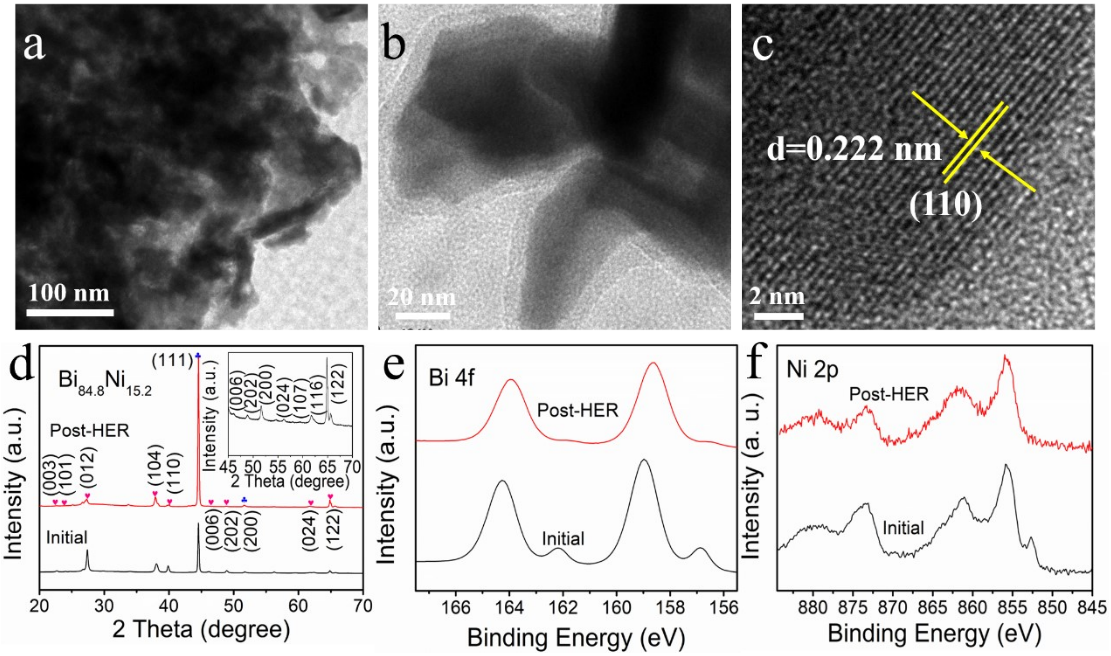

Fig. S12 Structural characterizations of $Bi_{84.8}Ni_{15.2}$ alloy after HER stability test (a-b) TEM; (c) HRTEM; (d) XRD; (e) Bi 4f and (f) Ni 2p before and after HER.

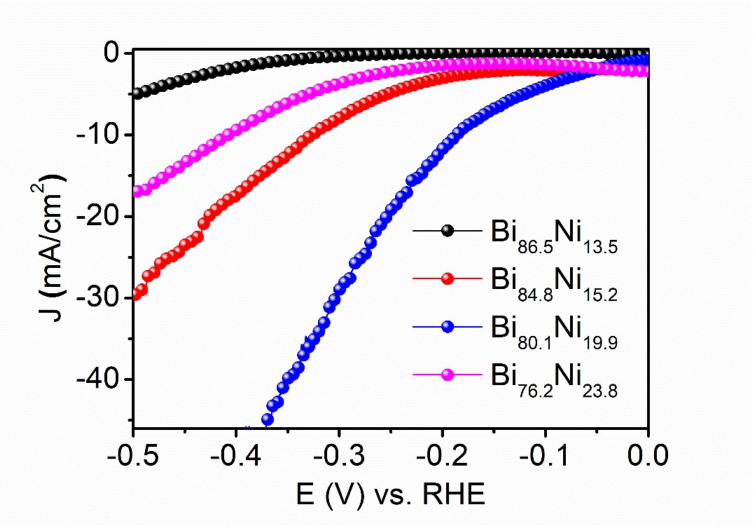

Fig. S13 Polarization curves of four alloys for HER in 1.0 M PBS (pH=7.0).

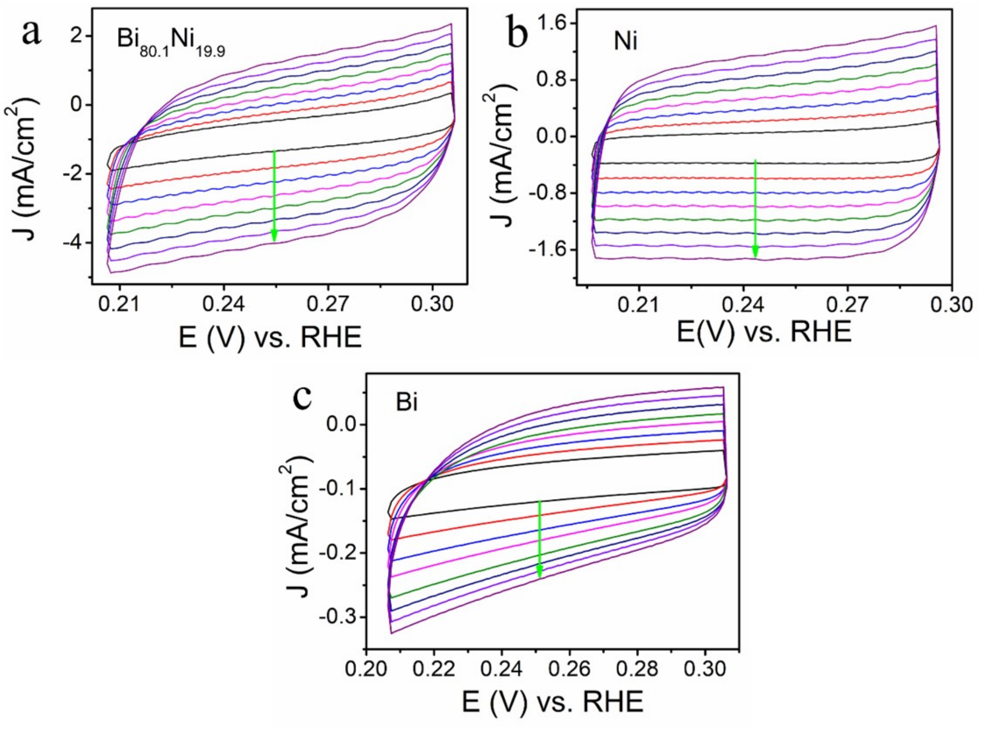

Fig. S14 CV (a) $Bi_{80.1}Ni_{19.9}$; (b) Ni; (c) Bi at 20-160 mV/s in 1.0 M PBS (pH=7.0).

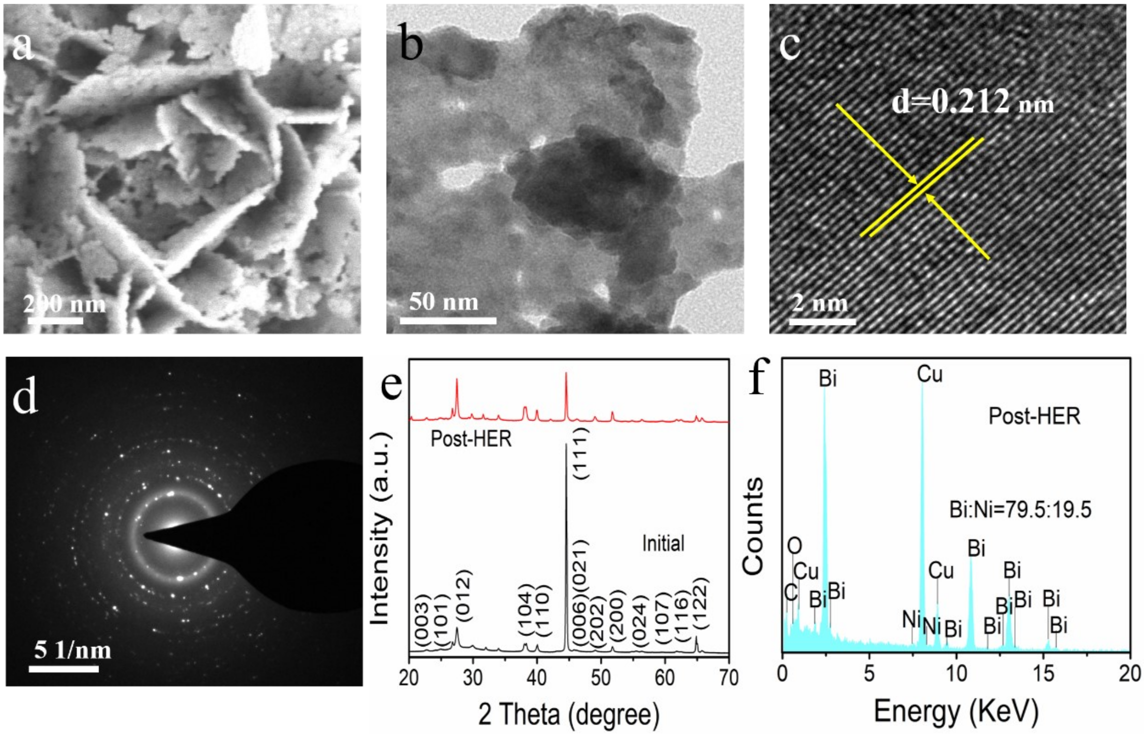

Fig. S15 Structural characterizations of $Bi_{80.1}Ni_{19.9}$ alloy after HER stability test (a) SEM; (b) TEM; (c) HRTEM (d) SAED; (e) XRD; (f) EDS spectrum.

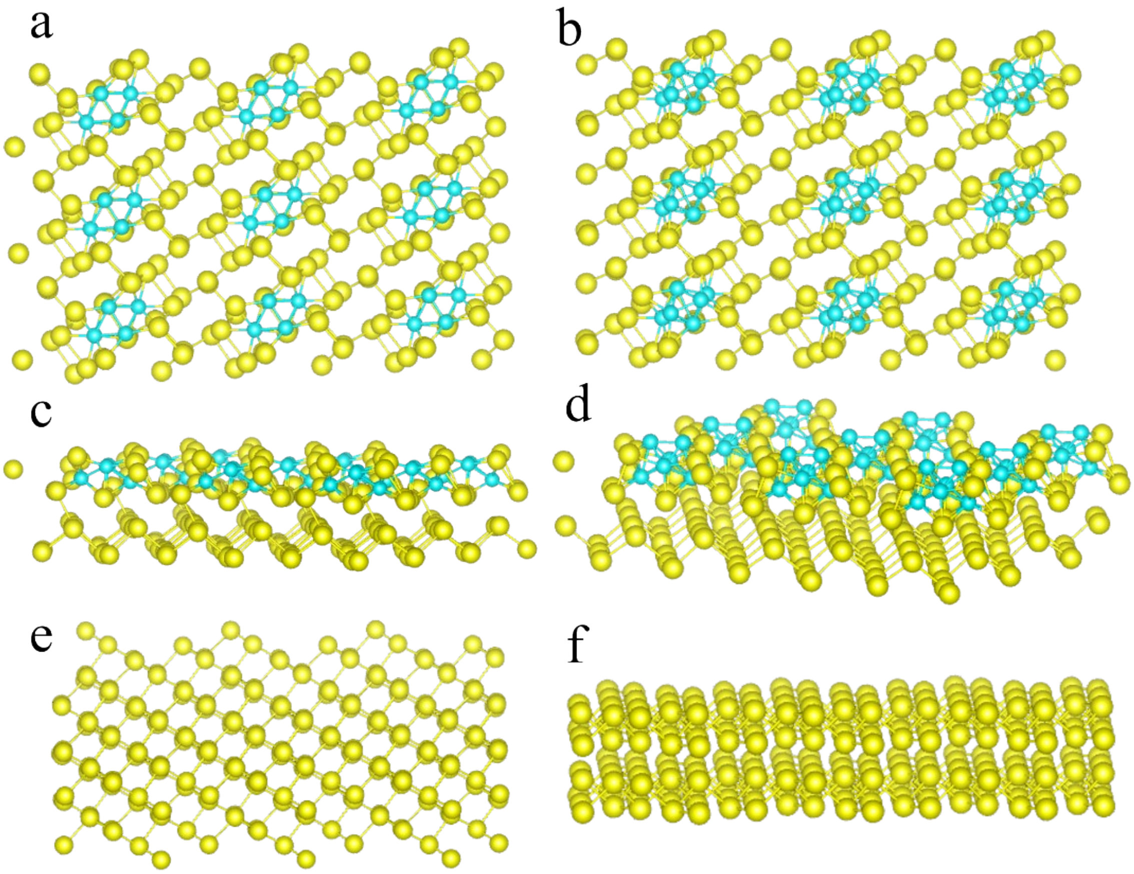

Fig. S16 Top view and side view of the models of (a, c) $Bi_{84.8}Ni_{15.2}$; (b, d) $Bi_{80.1}Ni_{19.9}$; (e, f) Bi.

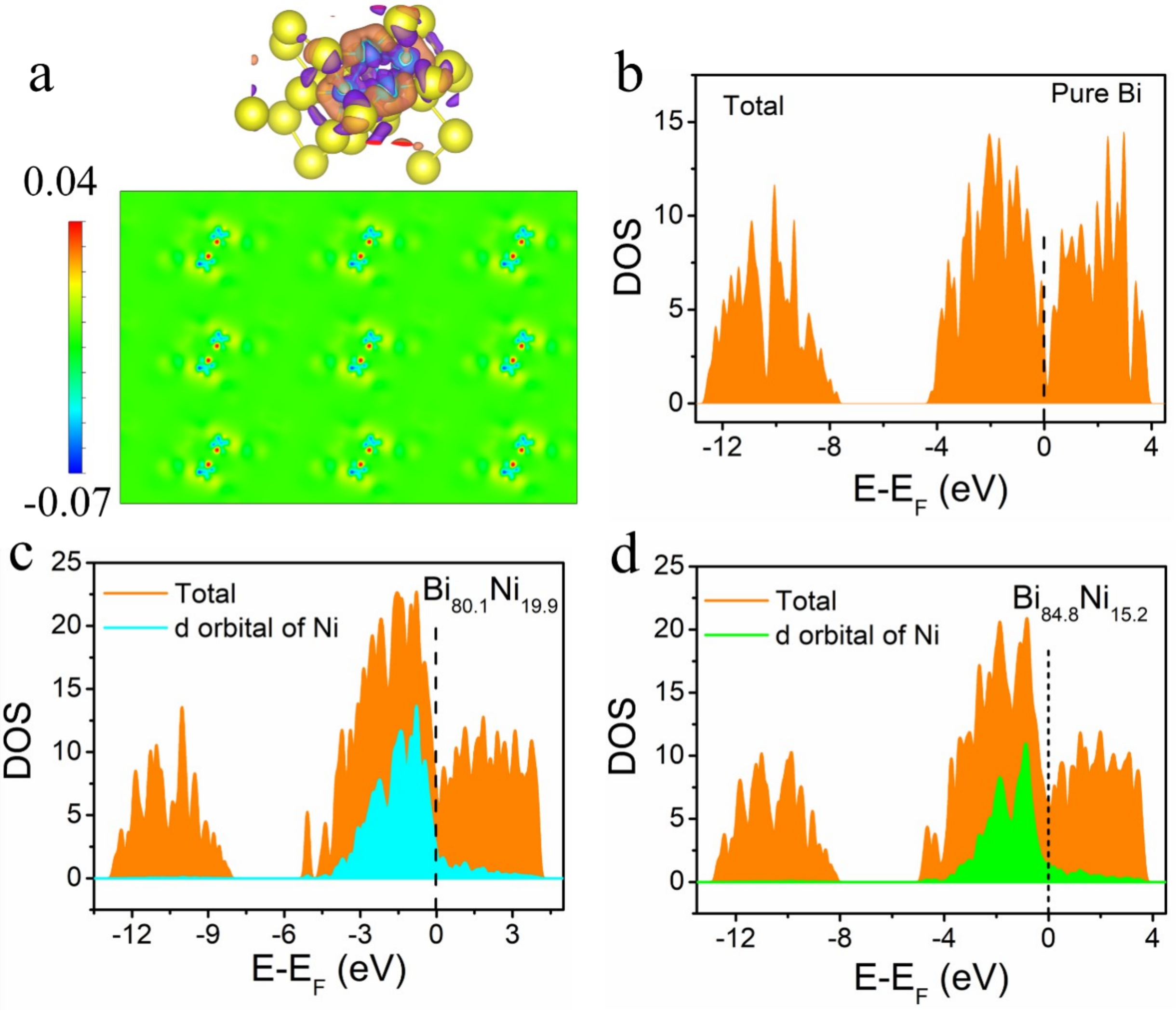

Fig. S17 (a) Top: Electron transfer in $Bi_{84.8}Ni_{15.2}$. Color: Yellow: Bi; cyan: Ni; orange and purple isosurfaces represent electron accumulation and electron depletion at an isosurface cutoff of 0.003 e-/Bohr^3. Bottom: Electron density change plots of $Bi_{84.8}Ni_{15.2}$; DOS of (b) Bi; (c) $Bi_{80.1}Ni_{19.9}$ alloy; (d) $Bi_{84.8}Ni_{15.2}$ alloy.

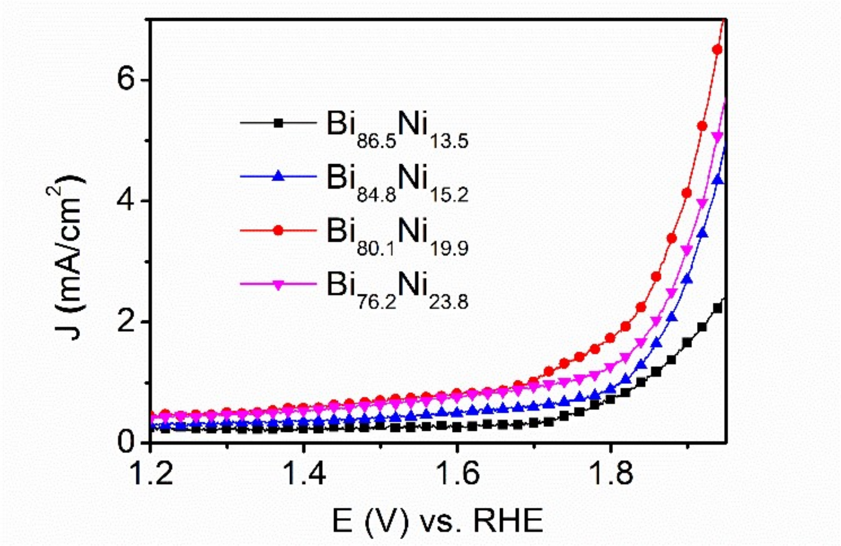

Fig. S18 Polarization curves of the four alloys for OER in 1.0 M PBS (pH=7.0).

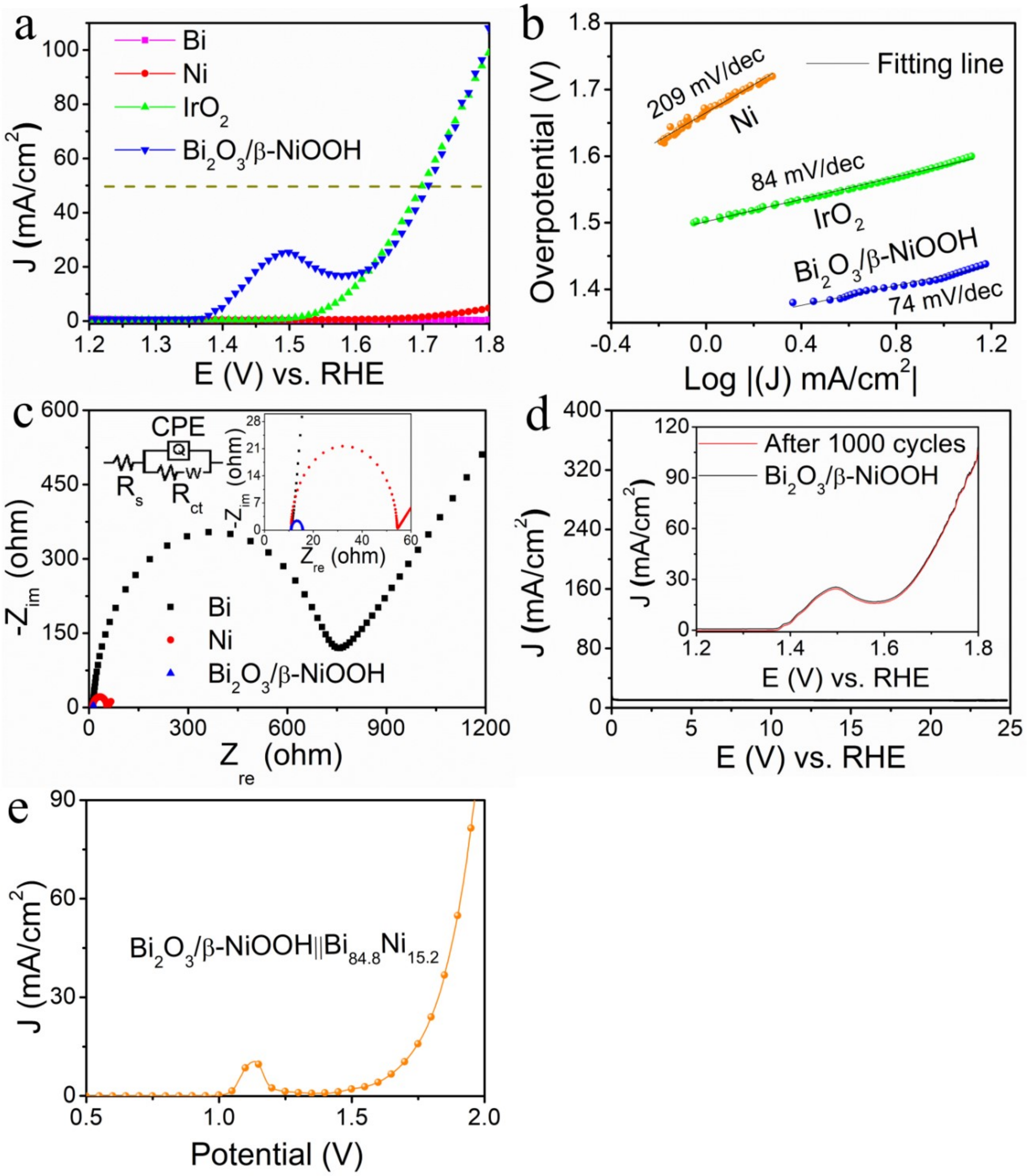

Fig. S19 (a) Polarization curves of samples for OER in 1.0 M KOH; (b) Tafel plots; (c) Nyquist plots at 1.4 V vs. RHE, inset is the magnification of the high-frequency region and equivalent circuit; (d) Durability test at 1.4 V vs. RHE, inset is the polarization curves of Bi_2O_3/β-NiOOH at 5 mV/s before and after 1000 cycles of CV.

To achieve a current density of 50 mA/cm^2, the required overpotentials are 479 mV and 470 mV for Bi_2O_3/β-NiOOH and IrO_2 for OER, respectively. Both Ni and Bi show negligible OER activity (Fig. S19a). Interestingly, the redox peaks of $Bi_{84.8}Ni_{15.2}$ alloy at 1.49 V vs. RHE corresponded to the transformation of Ni^{2+} to Ni^{3+}, which indicates substantial changes in the anodic peak potential (Fig. S19a). The area under the anodic peaks of $Bi_{86.5}Ni_{13.5}$, $Bi_{84.8}Ni_{15.2}$, $Bi_{80.1}Ni_{19.9}$ and $Bi_{76.2}Ni_{23.8}$ centered at 1.39, 1.49, 1.47 and 1.43 V are very different (Fig. S20a), which is mainly associated with NiOOH formation [17]. Fig. S20b revealed that the different atom ratio of Bi to Ni can have different influence on the OER activity. In Fig. S19b, Tafel slope of Bi_2O_3/β-NiOOH is 74 mV/dec, which is lower than mercantile IrO_2, Ni and Bi. Moreoever, the lower Tafel slope indicates faster electron kinetics of the water oxidation process on the surface of Bi_2O_3/β-NiOOH [17]. From Fig. S19 c, the charge transfer resistance of Bi_2O_3/β-NiOOH for OER is minimum, thus indicating its outstanding kinetics during OER process. In Fig. S21, the specific activity of Bi_2O_3/β-NiOOH is much shown to be much higher than Bi and Ni. These results demonstrate that Bi_2O_3/β-NiOOH not only increases the number of active sites, but also the increases the intrinsic catalytic activity. In Fig. S19d, the i-t measurements show no obvious decay at 10 mA/cm^2 for 25 h. No obvious change is observed when comparing the initial and final polarization curves after 1000 cycles of CV. This implies the excellent stability of Bi_2O_3/β-NiOOH.

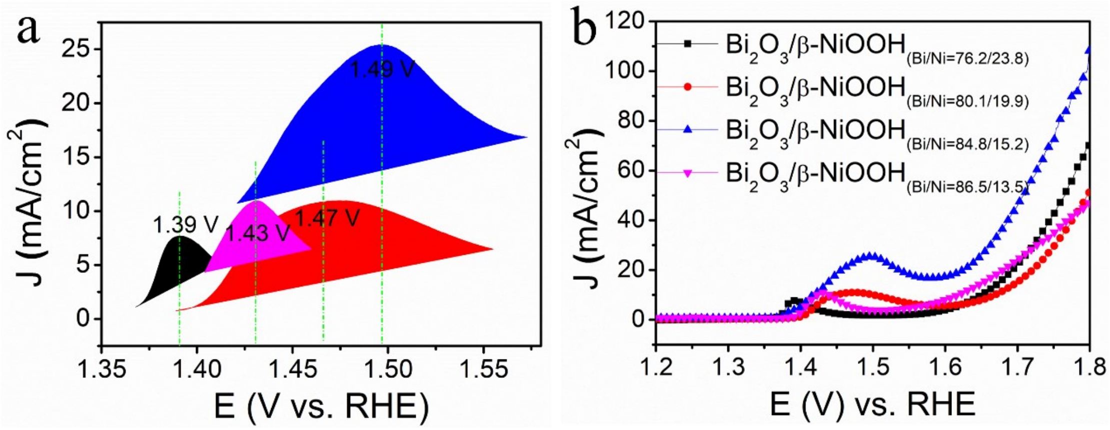

Fig. S20 (a) Polarization curves of the $Bi_{86.5}Ni_{13.5}$ (black), $Bi_{84.8}Ni_{15.2}$ (blue), $Bi_{80.1}Ni_{19.9}$ (red) and $Bi_{76.2}Ni_{23.8}$ (pink) showing the NiOOH formation peak used for area integration; (b) Polarization curves of different concentrations of Bi_2O_3/β-NiOOH catalysts for OER in 1.0 M KOH.

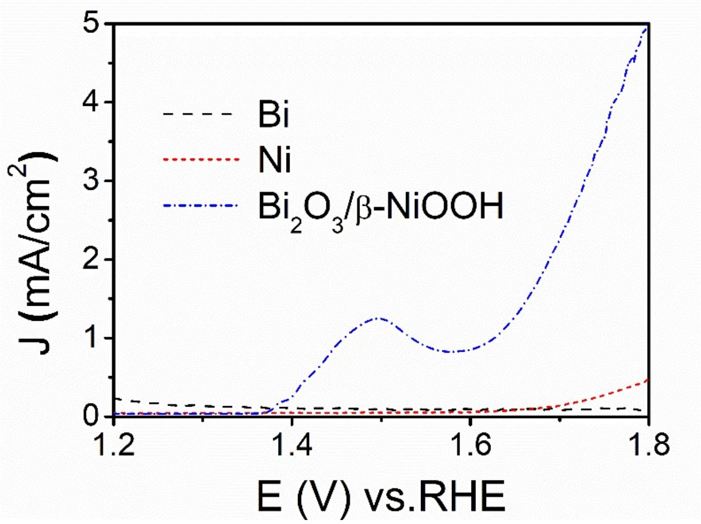

Fig. S21 (a) The specific activities of sample.

To further understand the OER process, the structure and surface state of post-OER catalyst are probed using various physical characterization. In Fig. S22a, the characteristic peaks for (003), (101), (012), (104) (110), (111), (006), (021), (202), (024) and (107) crystal facets disappear after electrolysis, the new peaks at 27.94, 33.83 and 54.25 degree are attributed to (201), (102) and (203) crystal facets of Bi_2O_3 (PDF#78-1793), and another peak at 37.84 degree is ascribed to the crystal facet (002) of β-NiOOH (PDF#15-0464). The result indicates that Bi_2O_3/β-NiOOH substances are formed during the OER process and this result is consistent with the polarization curves. There is an obvious change to the surface structure after the stability test (Fig. S22b,c), where the morphology becomes rather fluffy after OER testing. Furthermore, there are some defects on the surface of catalyst, which may be caused by the formation of new substance β-NiOOH (Fig. S22d). To some extent, these lattice defects may provide extra active sites, which will enhance the OER performance. In Fig. S22e, it can be seen that the peaks of Bi $4f_{5/2}$ and Bi $4f_{7/2}$ vanished while the peaks of Bi^{3+} are slightly shifted. These results indicate that Bi is completely transformed into Bi_2O_3. In Fig. S22f, the peak loaded at 852.6 eV disappeared after a 25 h electrolysis, while two new peaks at 857.4 eV and 874.4 eV appeared that correspond to Ni^{3+} of β-NiOOH, suggesting the existence of Ni^{3+} in the Ni 2p region [18]. Here, the results indicate the porous $Bi_{84.8}Ni_{15.2}$ alloy has undergone substantial changes and the main active substance on the surface of catalyst during the OER process is Bi_2O_3/β-NiOOH.

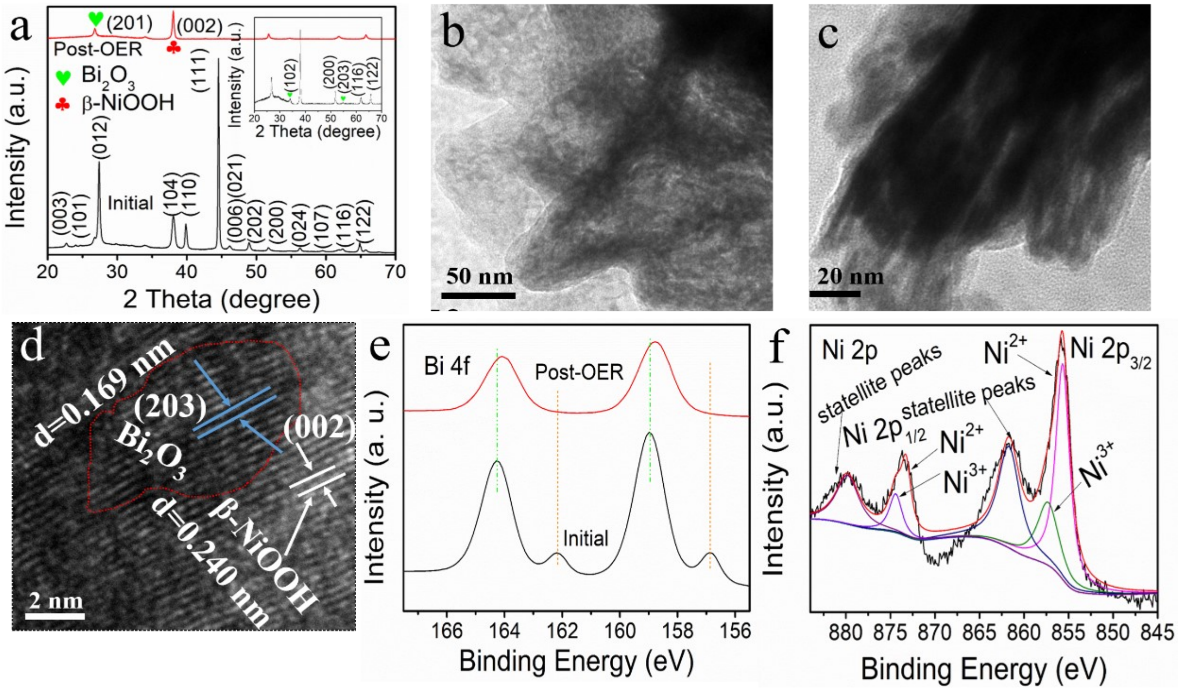

Fig. S22 Structural characterizations of Bi_2O_3/β-NiOOH (a) XRD before and after OER; (b-c) TEM; (d) HRTEM; (e) Bi 4f before and after OER; (f) Ni 2p.

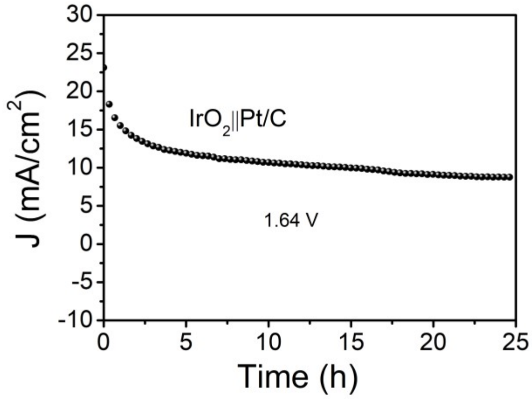

Fig. S23 I-t curve at constant cell voltage for IrO_2||Pt/C.

References

1. K. Fan, H. Chen, Y. F. Ji, H. Huang, P. M. Claesson, Q. Daniel, B. Philippe, H. Rensmo, F. S. Li, Y. Luo and L. C. Sun, *Nat Commun*, 2016, **7**, 11981.
2. X. Bai, Q. Q. Pang, X. Du, S. S. Yi, S. Zhang, J. Qian, X. Z. Yue and Z. Y. Liu, *Chem Eng J*, 2021, **417**, 129319.
3. Z. K. Du, Y. L. Wang, J. S. Li and J. P. Liu, *J Nanopart Res*, 2019, **21**, 13.
4. A. I. Inamdar, H. S. Chavan, B. Hou, C. H. Lee, S. U. Lee, S. Cha, H. Kim and H. Im, *Small*, 2020, **16**, 1905884.
5. H. J. Yu, Z. Q. Wang, Z. C. Dai, Q. Q. Mao, Y. Xu, X. N. Li, L. Wang and H. J. Wang, *Sustain Energ Fuels*, 2020, **4**, 4878-4883.
6. E. H. Eladgham, D. D. Rodene, R. Sarkar, I. U. Arachchige and R. B. Gupta, *Acs Appl Nano Mater*, 2020, **3**, 8199-8207.
7. Y. K. Bao, J. Y. Dai, J. Zhao, Y. Wu, C. Li, L. F. Ji, X. Zhang and F. C. Yang, *Acs Appl Energ Mater*, 2020, **3**, 1869-1874.
8. Q. Lu, G. S. Hutchings, W. Yu, Y. Zhou, R. V. Forest, R. Tao, J. Rosen, B. T. Yonemoto, Z. Cao, H. Zheng, J. Q. Xiao, F. Jiao and J. G. Chen, *Nat Commun*, 2015, **6**, 6567.
9. Y. Zhang, B. Ouyang, J. Xu, S. Chen, R. S. Rawat and H. J. Fan, *Adv Energy Mater*, 2016, **6**, 1600221.
10. Y. Tan, H. Wang, P. Liu, Y. Shen, C. Cheng, A. Hirata, T. Fujita, Z. Tang and M. Chen, *Energ Environ Sci*, 2016, **9**, 2257-2261.
11. Y. Yang, Z. Lun, G. Xia, F. Zheng, M. He and Q. Chen, *Energ Environ Sci*, 2015, **8**, 3563-3571.
12. L. J. Zhou, Z. X. Han, W. X. Li, W. X. Leng, Z. Yu and Z. Zhao, *J Alloy Compd*, 2020, **844**, 156108.
13. W. X. Zhang, Q. Jia, H. Liang, L. Cui, D. Wei and J. Q. Liu, *Chem Eng J*, 2020, **396**, 125315.
14. M. Q. Yao, B. J. Wang, N. Wang, S. Komarneni, Y. J. Chen, J. W. Wang, X. B. Niu and W. C. Hu, *Acs Sustain Chem Eng*, 2020, **8**, 5287-5295.
15. Z. Z. Xie, Y. Zou, L. J. Deng and J. Jiang, *Adv Mater Interfaces*, 2020, **7**, 901949.
16. W. Jin, H. B. Wu, W. Q. Cai, B. H. Jia, M. Batmunkh, Z. X. Wu and T. Y. Ma, *Chem Eng J*, 2021, **426**, 130762.
17. S. Anantharaj and S. Kundu, *Acs Energy Lett*, 2019, **4**, 1260-1264.
18. T. Tian, H. Gao, X. C. Zhou, L. R. Zheng, J. F. Wu, K. Li and Y. Ding, *Acs Energy Lett*, 2018, **3**, 2150-2158.